Research Square

Preprints are preliminary reports that have not undergone peer review.
They should not be considered conclusive, used to inform clinical practice,
or referenced by the media as validated information.

Bioinspired in-sensor orthogonal adaptation for robust all-weather multispectral vision

Furong Zhu

frzhu@hkbu.edu.hk

Hong Kong Baptist University https://orcid.org/0000-0002-6691-1937

Zhuangmiao Wang

Hong Kong Baptist University https://orcid.org/0009-0001-1498-6873

Songsong Li

University of Chicago https://orcid.org/0000-0001-9784-2877

Yu Tang

Hong Kong Baptist University https://orcid.org/0000-0002-2719-3119

Jiayin Han

Hong Kong Baptist University https://orcid.org/0000-0001-5718-278X

Mingsheng Gao

Shandong University https://orcid.org/0009-0007-6158-0132

Xuanyu Chen

Hong Kong Baptist University

Article

Keywords: bioinspired vision sensor, orthogonal adaption, multispectral vision, organic photodetector, in-sensor computing

Posted Date: March 26th, 2026

DOI: https://doi.org/10.21203/rs.3.rs-9082027/v1

License: This work is licensed under a Creative Commons Attribution 4.0 International License.
Read Full License

Additional Declarations: There is **NO** Competing Interest.

Bioinspired in-sensor orthogonal adaptation for robust all-weather multispectral vision

Zhuangmiao Wang†, Songsong Li†, Yu Tang, Jiayin Han, Mingsheng Gao, Xuanyu Chen, and Furong Zhu**

Department of Physics, Research Centre of Excellence for Organic Electronics, Institute of Advanced Materials, Hong Kong Baptist University, Kowloon Tong, Hong Kong, China

*Email: song2li@hkbu.edu.hk, frzhu@hkbu.edu.hku

†These authors contributed equally to this work.

Keywords: bioinspired vision sensor, orthogonal adaption, multispectral vision, organic photodetector, in-sensor computing

Abstract

Reliable machine vision under diverse illumination and weather conditions remains a major challenge for autonomous systems. Biological vision systems offer inspiration, utilizing distinct mechanisms for adapting to brightness and spectral composition. In this work, we report a bioinspired organic vision sensor with electrically switchable spectral response, enabling in-sensor orthogonal adaptation for robust multispectral imaging in all environments. The organic vision sensor transitions rapidly between photovoltaic mode for high-fidelity visible detection and photomultiplication mode for sensitive near-infrared imaging. This dual-mode operation supports robust vision performance in both bright and low-light scenarios, as well as in low-visibility conditions such as fog or haze. Experimental demonstrations and system-level simulations reveal substantial improvements in object detection under varying illumination and visibility. This approach establishes a foundation for adaptive multispectral imaging, advancing practical deployment of robotics, autonomous vehicles, and other electronic vision systems that require reliable performance in all-weather conditions.

Achieving robust multispectral vision in all-weather conditions is a critical bottleneck for the deployment of autonomous systems, from self-driving vehicles to intelligent robotics.[1,2] This bottleneck results from conventional image sensors, such as silicon (Si)-based complementary metal-oxide-semiconductor (CMOS) and charge-coupled device image sensors, which have a broadband spectral response and a static operational mode.[3-5] As a result, their performance is severely compromised by real-world environmental dynamics, presenting two key distinct challenges for autonomous vision: (1) achieving high-fidelity visible imaging and high-quality vision across extreme lighting conditions, from bright daylight to nocturnal darkness,[6,7] and (2) capturing high-contrast images under diverse weather and visibility scenarios, such as fog, haze, smoke and other adverse environments.[5] The inherent limitations of conventional vision sensor systems are typically mitigated by intensive post-processing.[8] While algorithms for high-dynamic-range imaging[9,10] and de-hazing[11] can improve data quality, their substantial computational demands often result in increased power consumption and latency.[8,12,13] These challenges hinder the practical use of such systems in power-sensitive applications requiring self-aligned imaging analysis and real-time monitoring.

Nature provides powerful insights for overcoming these limitations through biological adaptation (**Fig. 1**).[14] To tackle extreme variations in illumination, the human retina employs a duplex system, dynamically transitioning between high-sensitivity rod photoreceptors for scotopic (dark-adapted) vision and high-fidelity cone photoreceptors for photopic (light-adapted) vision (**Fig. 1a-c**).[14,15] This principle of illumination adaptation has inspired artificial vision sensors that can modulate their sensitivity to handle high-dynamic-range scenes.[6] Migratory species such as

Pacific salmon have evolved specialized spectral adaptation that enable them to detect critical environmental features even under low-visibility conditions (**Fig. 1d-f**).[16] By enzymatically altering their visual pigments, e.g., switching between Vitamin A_1-based visual pigment (VP1), optimized for shorter wavelength sensitivity in clear water and Vitamin A_2-based visual pigment (VP2), optimized for longer wavelength sensitivity in turbid water, these species shift their spectral sensitivity to optimize visual contrast under changing environmental conditions.[17] These biological adaptations have inspired the development of vision sensors that can individually mimic either illumination adaptation[6,18-24] or spectral adaptation.[5,7,25-29] However, a monolithic vision sensor that can unify both functions, e.g., orthogonally adapting its spectral response and sensitivity to achieve robust multispectral vision in all-weather conditions, has yet to be realized.

In this work, we introduce a bioinspired organic vision sensor that achieves in-sensor orthogonal adaptation for accurate all-weather multispectral vision (**Fig. 1g-i**). Our bioinspired organic vision sensor is based on a back-to-back stacked photovoltaic (PV)/photomultiplication (PM) double bulk heterojunction organic photodetector (PV/PM-OPD) array. The front PV junction responds to short-wavelength (visible) light, whereas the rear PM junction responds to near-infrared (NIR) light. The use of a dual-mode PV/PM-OPD helps to enhance NIR responsivity through PM effect, due to the trap-assisted charge injection at the PM junction/cathode interface under a reverse bias.[30-34] The double heterojunction PV/PM-OPD allows a multispectral detection that is controlled by the polarity of a bias voltage applied between the two contacts in the device.[5,35-39] When a reverse bias is applied across the PV/PM-OPD electrodes, the front PV junction conducts passively while the rear PM junction, in reverse bias, selectively detects NIR

light. This mode mimics the high sensitivity of scotopic (dark-adapted) vision and utilizes the PM effect to enhance spectral response in the NIR region, a challenge for current multispectral OPDs. Conversely, under a forward bias, the organic vision sensor switches to PV mode for high-fidelity visible imaging, analogous to photopic (light-adapted) vision for bright daylight spectral response. The switching between PV mode (light-adapted vision) to PM mode (dark-adapted or low-visibility vision) occurs in ~30 μs, offering a speed advantage orders of magnitude faster than biological spectral adaptation. We validate this concept on a 4 × 4 sensor array, demonstrating experimentally that orthogonal adaptation significantly enhances pattern-recognition accuracy across varying illuminance levels and improves image contrast in diverse visibility environments. Complementary system-level simulations further demonstrate the practical utility of the bioinspired dual-mode organic vision sensor in realistic night-driving and low-visibility scenarios, confirming its potential to provide robust multispectral vision in all-weather conditions.

Spectral responses of PV/PM-OPD

Currently, commercial image sensors predominantly rely on broadband photodetectors, such as Si p-n junction photodiodes operated in PV mode for standard detection,[40,41] and Si avalanche photodiodes for applications requiring high-gain sensing.[42,43] However, the broadband spectral response of the Si photodiodes limits their adaptability in dynamic environments. To enable robust multispectral vision in all-weather conditions, we developed a back-to-back stacked monolithic PV/PM-OPD capable of electrically switching between PV and PM modes (**Fig. 2a**). It integrates a 450 nm-thick visible-light-absorbing front PV junction, prepared using a blend solution of poly(3-hexylthiophene) (P3HT) and [6,6]-phenyl-C71-butyric acid methyl ester ($PC_{71}BM$) with a weight ratio of P3HT to $PC_{71}BM$ of 1:1, and a 500 nm-thick NIR-absorbing rear PM junction, prepared using a blend solution of poly[(4,8-bis(5-(2-ethylhexyl)thiophen-2-yl)benzo[1,2-b:4,5-b']dithiophene)-alt-(3-fluorothieno[3,4-b] thiophene)] (PBDB-T) and 2,2'-((2Z,2'Z)-((12,13-Bis(2-ethylhexyl)-3,9-diundecyl-12,13-dihydro-[1,2,5]thiadiazolo [3,4-e]thieno[2",3'':4', 5'] thieno[2',3':4,5] pyrrolo [3,2-g]thieno[2',3':4,5]thieno[3,2-b]indole-2,10-diyl)bis (methanylylidene))bis(5,6-difluoro-3-oxo-2,3-dihydro-1H-inde (Y6) with a weight ratio of PBDB-T to Y6 of 100:3. The front PV and rear PM junctions are connected by a 60 nm-thick floating copper thiocyanate (CuSCN) anode layer. The schematic diagram of the energy levels of the functional materials used in the PV/PM-OPD are shown in **Fig. 2b**. The molecular structures and the normalized absorption spectra of the active materials are shown in **Supplementary Fig. 1**. It shows that the absorption of the P3HT:$PC_{71}BM$ (1:1)-based photoactive layer covers the wavelength range from 300 to 650 nm, while that of the PBDB-T:Y6 (100:3)-based light absorbing

layer extends to 900 nm. The profile of the optical field distribution in the P3HT:$PC_{71}BM$/PBDB-T:Y6-based double heterojunction PV/PM-OPD was analyzed using optical admittance analysis.[33,44] The wavelength-dependent refractive indices (n) and extinction coefficients (k) of the functional layers used in the optical simulation are shown in **Supplementary Fig. 2**.[33,44] The resulting absorbed photon distribution (**Fig. 2c**) demonstrates that the short-wavelength photons with wavelength below 650 nm are absorbed within the 450 nm thick front PV layer, while long-wavelength photons with wavelength above 650 nm are captured by the 500 nm thick rear PM junction. Consequently, the front PV junction functions simultaneously as a high-fidelity visible detector and as an intrinsic optical filter that shields the rear PM junction from visible interference.

The PV/PM double heterojunction design allows the spectral-adapted responses by adjusting the polarity of the bias across the device. As shown in **Fig. 2d**, the PV/PM-OPD adapts dynamically between two distinct modes. For example, under a forward bias of 5 V, the device operates in PV mode, delivering high-fidelity visible spectral response from 300 to 650 nm and achieving a peak external quantum efficiency (EQE) of 45% at 515 nm. When it is operated under a reverse bias of −10 V, the OPD switches to its PM mode, exhibiting a distinct spectral response in the long wavelength range of 650 to 900 nm. In PM mode, the EQE reaches 180% at 810 nm, far exceeding the unity, enabled by the trap-assisted charge injection effect, thus providing an extremely high photosensitivity to NIR.[45,46] The thickness and composition of the PBDB-T:Y6-based PM junction in the dual-mode PV/PM-OPD was optimized using PBDB-T:Y6 blend solution with a weight ratio of PBDB-T to Y6 100:3 (**Supplementary Fig. 3**). The spectral selectivity of the P3HT:$PC_{71}BM$ (1:1)/PBDB-T:Y6 (100:3)-based dual-mode PV/PM-OPD was

optimized by independently enhancing the performance of discrete P3HT:$PC_{71}BM$-based PV and PBDB-T:Y6-based PM control OPDs. The characteristics of the individual PV and PM control devices are presented in **Supplementary Fig. 4**. The PV/PM double heterojunction design with enhanced NIR response for multispectral detection can also be adopted using various combinations of front PV and rear PM junctions. For instance, a dual-mode PV/PM-OPD, combined with a front P3HT:$PC_{71}BM$ (1:1)-based PV junction and a rear P3HT:PTB7-Th:$PC_{71}BM$ (70:30:1)-based PM junction, enables bias-switchable, spectrally selective detection across both short-wavelength (300 to 650 nm) and long-wavelength (650 to 800 nm) ranges. The device characteristics of the P3HT:$PC_{71}BM$/P3HT:PTB7-Th:$PC_{71}BM$-based PV/PM-OPD are presented in **Supplementary Fig. 5**. It shows that this dual-mode OPD has a specific detectivity (D^*) of approximately 10^{12} Jones in both bands (**Supplementary Fig. 6**), demonstrating the versatility of the double heterojunction design strategy for multispectral detection and self-aligned imaging across distinct spectral bands.[3335,37]

The schematic diagrams illustrating the mechanism of the spectral selective responses of the PV/PM-OPD are shown in **Fig. 2e**. Under forward bias, the front PV junction is at its reverse-biased condition, producing a photocurrent by absorbing short-wavelength (visible) light, while the rear PM junction is under its forward conduction state, passively conducting current. Conversely, under reverse bias, the front PV junction is at its forward conduction state passively conducting current, whereas the rear PM junction is at its reverse-biased condition state, producing a photocurrent by absorbing the long-wavelength (NIR) part of the incoming light. The use of PV/PM-type OPDs enables spectral selectivity for multispectral detection by leveraging the

complementary absorption properties of two heterojunctions. In this device architecture, the front PV junction also acts as a built-in filter that efficiently absorbs visible light, while the rear PM junction is responsible for detecting the long-wavelength (NIR) portion of the incident light. The device further benefits from the PM effect, which enhances sensitivity at longer wavelengths. By integrating this dual heterojunction structure, the PV/PM-OPD achieves distinctive spectrally selective responses, most notably, improved performance in the long-wavelength region, effectively addressing a key limitation of conventional single-mode broadband photodetectors that rely on bandpass or multiple optical filters.[47-51]

Characteristics of dual-mode PV/PM-OPD

The current density–voltage (*J–V*) characteristics, measured for the P3HT:$PC_{71}BM$/PBDB-T:Y6-based PV/PM-OPD under visible (515 nm) and near-infrared (810 nm) illumination, are shown in **Fig. 3a**. Photoresponses measured for the dual-mode PV/PM-OPD in PV mode (5 and 10 V) under illumination of visible light (515 nm, 6.3 μW) and in PM mode (-5 and -10V) under illumination of NIR light (810 nm,1.4 μW) are shown in **Supplementary Fig. 7**. The response speed of the dual-mode PV/PM-OPD, a key parameter for use in real-time multispectral vision system,[52] was characterized under both modes using modulated illumination. In PV mode (5 V), the device was tested with a 100 Hz modulated visible light (515 nm, 6.3 μW), yielding a rise time (τ_r) of 0.31 ms and a fall time (τ_f) of 0.12 ms. Under PM mode (−10 V) with a 100 Hz modulated NIR source (810 nm, 1.4 μW), the device exhibited a τ_r of 1.62 ms and a τ_f of 0.55 ms, as shown in **Fig. 3b**. The dual-mode PV/PM-OPD exhibits a −3 dB cutoff frequency of 700 Hz in PV mode

(5 V), and greater than 300 Hz in PM mode (−10 V), as shown in **Supplementary Fig. 8**. Rapid electrical reconfiguration was achieved, with switching times of 34 μs from PM to PV mode, and 30 μs in the reverse direction, as shown in **Fig. 3c**, corresponding to a reconfiguration rate exceeding 10,000 cycles per second. This is orders of magnitude faster than the switching speeds found in human vision (photopic/scotopic) and biological vision systems enabled by spectral adaptation (VP1/VP2) (**Fig. 1c, f**). Long-term operational stability was also demonstrated, as stable photocurrents were maintained under repeated illumination in both modes over 7200 s, as shown in **Fig. 3d** and **Supplementary Fig. 9**. These results confirm that the bias-switchable dual-mode PV/PM-OPD offers fast, robust, and spectrally consistent performance in both the visible and NIR regions.

The linear dynamic range (LDR) of the device in both modes, defined as the range over which the photocurrent is linearly proportional to the incident light intensity[53,54], was analyzed. As shown in **Fig. 3e**, the PV mode exhibits an LDR of 101 dB, covering input intensities from 2.72×10^{-10} to 1.98×10^{-3} W/cm^2, thereby enabling high-fidelity visible light imaging. Similarly, the PM mode achieves an LDR of 94 dB and supports the detection of NIR light at low intensities down to 1.59×10^{-10} at 810 nm, outperforming conventional silicon CMOS image sensors (70 dB).[6] The spectral responses of the PV/PM-OPD operated in PV mode (5 V) and in PM mode (-10 V) were also evaluated under a white LED light source with illuminance ranging from 8.4×10^{-3} to 1.2×10^{3} lux. The ratio of photocurrent density (J_{light}) to dark current density (J_{dark}) (J_{light}/J_{dark}), measured for the dual-mode PV/PM-OPD under white light with varying illuminance from 8.4×10^{-3} to

1.2×10^3 lux under a constant exposure time of 20 s, was analysed, the results are shown in **Fig. 3f**. It shows that the PM mode exhibits a higher J_{light}/J_{dark} ratio across the entire range of illuminance values, suggesting the ability of high contrast image that can be taken by the PM mode under varying illuminance, supported by the analysis of the J_{light}/J_{dark} ratios obtained under white light with varying illuminance (**Supplementary Fig. 10**).

Illumination adaptation of dual-mode vision sensor for pattern recognition

A 4 × 4 sensor array of PV/PM-OPD vision sensors was developed to demonstrate the illumination adaptation capabilities of the PV/PM-OPD for pattern recognition under varying luminance and visibility conditions. The array exhibits an excellent pixel-to-pixel uniformity in currents measured in dark and different lighting conditions, along with a high operational stability (**Supplementary Fig. 11-12**). A spectral crosstalk of about 7.8% was observed between adjacent organic vision sensor pixels (**Supplementary Fig. 13**), which is attributed to the limited lateral carrier diffusion in the organic active layers. This low crosstalk ensures the high spatial resolution and suitability of the organic vision sensor for reliable pattern recognition under varying environmental conditions. Using this array, we performed an imaging experiment by projecting an "H"-shaped pattern under varying illumination conditions (**Fig. 4a**). A rigorous testing protocol involving six distinct signal light intensities of dark, 4.4×10^{-2}, 0.5, 6.3, 2.8×10^2, and 1.4×10^3 lux was adopted to simulate realistic environmental dynamics. The background light for each measurement, set to select the intensity of the preceding level, e.g., a 4.4×10^{-2} lux background for a 0.5 lux signal, and a 2.8×10^2 lux background for a 1.4×10^3 lux signal, was used to mimic the varying contrast of real-world scenes. The resulting signal-to-noise ratio (SNR) evolution is

presented in **Fig. 4b**. Detailed SNR analysis under fixed background conditions further supports this trend (**Supplementary Fig. 14**). Apart from the SNR, we also evaluated the image quality using root mean square (RMS) contrast. These results consistently show that the PM mode (-10 V) yields superior contrast in low-light regimes (4.4×10^{-2} to 6.3 lux), whereas the PV mode (5 V) outperforms the PM mode as light intensity increases to daylight levels (**Supplementary Figs. 15-16**). The reconstructed current maps visually confirm the necessity of this adaptation. Under simulated dark-adapted vision conditions (0.5 lux signal against 4.4×10^{-2} lux background), the PM mode clearly resolves the "H" pattern, whereas the PV mode yields a blurred, low-contrast image due to insufficient sensitivity (**Fig. 4c**). In contrast, under light-adapted conditions (1.4×10^{3} lux signal against 2.8×10^{2} lux background), the PV mode delivers high-fidelity imaging, effectively extracting the pattern from the bright background (**Fig. 4d**). The complete set of experimental mappings under various signal-to-background combinations is provided in **Supplementary Fig. 17**.

System-level simulations, based on a complex traffic scenario containing five object classes of bicycle, car, face, barrier, and streetlight (**Fig. 4e**), were conducted evaluating the impact of this hardware-level adaptation on downstream machine vision tasks. A neural network classifier (**Fig. 4f**) was trained on the binary "Quick Draw!" dataset to establish baseline recognition capabilities. Then, during the inference phase, the trained model processed images generated by randomly sampling pixel current values from the experimental results corresponding to each specific illumination scenario (**Supplementary Fig. 18**). As shown in **Fig. 4g**, classification accuracy is highly dependent on the operational mode. The PM mode maintains high accuracy (>95%) in low-

light environments where the PV mode performance degrades significantly to 60% (**Supplementary Fig. 19**). However, as illumination increases, the PV mode becomes essential for maintaining recognition accuracy (**Supplementary Fig. 20**). Representative simulation outputs (**Fig. 4h, i**) demonstrate that selecting the correct adaptive mode, utilizing PM for dark-adapted vision and PV for light-adapted vision, is critical for achieving recognizable features and achieving robust all-weather multispectral vision in autonomous systems.

Spectral adaptation for robust vision in low-visibility conditions

Beyond illumination adaptation, the ability to maintain high-sensitivity spectral response in low-visibility environmental conditions, such as fog, haze, or smoke, is also critical for robust all-weather multispectral vision. To validate the spectral adaptation capability of the bioinspired organic vision sensor, designed to mimic the biological vision strategy of the Pacific salmon in changing environmental conditions, we conducted experiments to assess imaging performance under varying levels of turbidity. Different turbid visibility conditions were simulated by dispersing silica nanoparticles (Si-NPs) with an average diameter of 1 μm in solution, at concentrations ranging from 0 to 25 mg/mL (**Fig. 5a**). By varying the concentration of the Si-NPs in the scattering medium placed over an array of 4 × 4 organic vision sensors, spectral adaptation ability of the sensor array to image target patterns under increasing turbidity was analyzed. The fundamental advantage of orthogonal adaptation for robust multispectral vision in all weather conditions lies in the wavelength-dependent nature of scattering. According to scattering theory, the scattering cross-section is inversely related to the wavelength. Therefore, long wavelength NIR light experiences significantly less attenuation and scattering than visible light. As a result, the

organic sensor array operated in PM mode captures clearer images of the target pattern under turbid conditions compared to its performance in PV mode. The advantage of the dual-mode PV/PM-OPD for high-quality imaging in distinct bands is experimentally verified (**Fig. 5b** and **Supplementary Fig. 21**). Under visible light illumination (515 nm), the sensor array operated in PV mode exhibits an order of magnitude decrease in photocurrent as the concentration of Si-NPs in the solution increases (**Supplementary Table 1**). This reduction is attributed to increased scattering of visible light by the Si-NPs within the medium. In contrast, when illuminated with NIR light (810 nm) and operated in PM mode, the sensor array maintains a relatively stable photocurrent across the Si-NP concentration range of 0 to 25 mg/mL, revealing its superior NIR imaging capability in PM mode. The analysis of RMS contrast of images captured under both PV and PM modes, as a function of Si-NP concentration in the scattering medium, is presented in **Supplementary Fig. 22**. The reconstructed current maps (**Supplementary Fig. 23**) visually confirm this capability, showing that in PM mode, images exhibit higher SNR and RMS contrast compared to in PV mode at high Si-NP concentrations.

System-level simulations of vehicle detection under foggy conditions (**Fig. 5c**) were conducted to assess the practical applications of this capability for autonomous systems. High-visibility images were processed using the Koschmieder's light scattering model[55] to generate inputs with varying scattering coefficients (β), which were then fed into the models[56] of our dual-mode vision sensor before being analyzed by the YOLOv8 object detection algorithm[57,58]. The detection accuracy as a function of the scattering coefficient is presented in **Fig. 5d**. The results show a clear contrast in performance, as the detection accuracy of the PV mode decreases rapidly with

decreasing visibility, dropping to zero at a β of 0.08. In contrast, the PM mode maintains an accuracy of over 60% even under severe scattering conditions where the PV mode fails completely. When operating in PV mode, vehicles become indistinguishable in PV mode due to the poor contrast (**Fig. 5e**). However, in PM mode, pattern recognition remains robust, allowing critical feature information to be recovered (**Fig. 5f**). This allows the neural network to successfully locate and classify the vehicles, confirming its in-sensor orthogonal adaptation for high-quality imaging in challenging low-visibility conditions.

A comparative summary of device performance, including single-mode photodetectors designed for either spectral or illumination adaptation from various research groups, as well as the bioinspired dual-mode PV/PM-OPD developed in this work, is presented in **Supplementary Table 2**. The PV/PM-OPD demonstrates a unique bias-switchable spectral responses. In PV mode, it achieves high-sensitivity visible spectral response, mimicking photopic (light-adapted) human vision under bright conditions. In PM mode, the vision sensor exhibits enhanced sensitivity in the NIR region, especially under low-visibility conditions, due to the PM effect. This behaviour is analogous to scotopic (dark-adapted) vision, enabling improved performance in dark environments. This adaptive robust multispectral sensing capability represents a substantial advancement over existing single-mode photodetectors, offering dynamic spectral response control that is currently unattainable with conventional technologies.

Conclusions

In summary, we have demonstrated a bioinspired monolithic dual-mode organic vision sensor capable of orthogonal adaptation to both illumination and spectral changes. By electrically

switching between a high-fidelity visible PV mode and a high-gain NIR PM mode, the vision sensor overcomes the intrinsic limitations of the conventional static imagers. This dual-mode vision sensor not only enables robust multispectral vision in high-dynamic-range spanning from bright daylight to nocturnal darkness but also effectively penetrates the scattering medium to recover visual information in low-visibility conditions. The microsecond-scale reconfiguration speed between PV (light-adapted vision) to PM (dark-adapted or low-visibility vision) mode allows for real-time adaptability that far exceeds biological spectral adaptation capabilities. By bridging the gap between biological inspiration and innovative device design, this work marks a significant step forward in all-weather multispectral machine vision technologies.

Acknowledgments

This work was financially supported by the Research Grants Council (GRF/12302623, 12304024, 12304225), Hong Kong Innovation and Technology Commission (GHP/121/21GD), Hong Kong Special Administrative Region, China, and Guangdong Basic and Applied Basic Research Fund (2022A1515010020), China. S. Li acknowledges support from the start-up fund (No.179552) provided by Hong Kong Baptist University.

Author contributions

F.Z. supervised the execution of the project. Z.W. designed and fabricated the device. Z.W. and Y.T. performed the device characterization. S.L. guided the fabrication and testing of the sensor array, analyzed the array data, and conducted the machine vision simulations. J.H., M.G., and X.C. contributed to the analysis of the results. Z.W., S.L., and F.Z. wrote the manuscript. All authors participated in the discussions for manuscript preparation.

Code availability

The codes used for machine vision simulations are available via Github at https://github.com/song2li/orthogonal-adaptation.

Competing interests

The authors declare no competing financial interests.

Additional Information

Supplementary Information is available in the online version of the paper.

Correspondence and requests for materials should be addressed to S. L. and F.Z. (song2li@hkbu.edu.hk; frzhu@hkbu.edu.hku)

References

1 Zang, S. *et al.* The impact of adverse weather conditions on autonomous vehicles: How rain, snow, fog, and hail affect the performance of a self-driving car. *IEEE vehicular technology magazine* **14**, 103-111 (2019).
2 Raut, R., Krit, S. & Chatterjee, P. *Machine Vision for Industry 4.0: Applications and Case Studies*. (CRC Press, 2022).
3 Dudek, P. *et al.* Sensor-level computer vision with pixel processor arrays for agile robots. *Science robotics* **7**, eabl7755 (2022).
4 Mennel, L. *et al.* Ultrafast machine vision with 2D material neural network image sensors. *Nature* **579**, 62-66 (2020).
5 Ouyang, B. *et al.* Bioinspired in-sensor spectral adaptation for perceiving spectrally distinctive features. *Nat. Electron.* **7**, 705-713 (2024).
6 Liao, F. *et al.* Bioinspired in-sensor visual adaptation for accurate perception. *Nat. Electron.* **5**, 84-91 (2022).
7 Tan, Z. *et al.* Bias-switchable dual-mode organic photodetectors for spectrally adaptive vision and secure encoding. *Materials Today* (2025).
8 Almalioglu, Y., Turan, M., Trigoni, N. & Markham, A. Deep learning-based robust positioning for all-weather autonomous driving. *Nature machine intelligence* **4**, 749-760 (2022).
9 Banterle, F., Artusi, A., Debattista, K. & Chalmers, A. *Advanced high dynamic range imaging*. (AK Peters/CRC Press, 2017).
10 Li, C. in *2024 3rd International Conference on Automation, Robotics and Computer Engineering (ICARCE).* 152-156 (IEEE).

11 Zheng, C., Ying, W. & Hu, Q. Comparative analysis of dehazing algorithms on real-world hazy images. *Scientific Reports* **15**, 10822 (2025).
12 Zhou, F. & Chai, Y. Near-sensor and in-sensor computing. *Nature Electronics* **3**, 664-671 (2020).
13 Gehrig, D. & Scaramuzza, D. Low-latency automotive vision with event cameras. *Nature* **629**, 1034-1040 (2024).
14 Choi, C., Lee, G. J., Chang, S., Song, Y. M. & Kim, D. H. Inspiration from Visual Ecology for Advancing Multifunctional Robotic Vision Systems: Bio‐inspired Electronic Eyes and Neuromorphic Image Sensors. *Advanced Materials* **36**, 2412252 (2024).
15 Kandel, E. R. *et al. Principles of neural science*. Vol. 4 (McGraw-hill New York, 2000).
16 Carleton, K. L., Escobar-Camacho, D., Stieb, S. M., Cortesi, F. & Marshall, N. J. Seeing the rainbow: mechanisms underlying spectral sensitivity in teleost fishes. *Journal of Experimental Biology* **223**, jeb193334 (2020).
17 Corbo, J. C. Vitamin A1/A2 chromophore exchange: Its role in spectral tuning and visual plasticity. *Developmental Biology* **475**, 145-155 (2021).
18 Zhang, M. *et al.* An Irradiance-Adaptable Near-Infrared Vertical Heterojunction Phototransistor. *Adv Mater* **34**, e2205679 (2022).
19 Shi, L. *et al.* Flexible retinomorphic vision sensors with scotopic and photopic adaptation for a fully flexible neuromorphic machine vision system. *SmartMat* **5** (2024).
20 He, Z. *et al.* An organic transistor with light intensity-dependent active photoadaptation. *Nat. Electron.* **4**, 522-529 (2021).
21 Kwon, S. M. *et al.* Environment-Adaptable Artificial Visual Perception Behaviors Using a Light-Adjustable Optoelectronic Neuromorphic Device Array. *Adv Mater* **31**, e1906433 (2019).
22 Gong, G. *et al.* An Antagonistic Photovoltaic Memristor for Bioinspired Active Contrast Adaptation. *Adv Mater* **36**, e2409844 (2024).
23 Li, L. *et al.* Adaptative machine vision with microsecond-level accurate perception beyond human retina. *Nat Commun* **15**, 6261 (2024).
24 Wang, C. *et al.* Strain-insensitive viscoelastic perovskite film for intrinsically stretchable neuromorphic vision-adaptive transistors. *Nat Commun* **15**, 3123 (2024).
25 Gong, G. *et al.* Bioinspired Adaptive Sensors: A Review on Current Developments in Theory and Application. *Adv Mater*, e2505420 (2025).
26 Hong, S. *et al.* Sensory Adaptation and Neuromorphic Phototransistors Based on CsPb(Br(1-x)I(x))(3) Perovskite and MoS(2) Hybrid Structure. *ACS Nano* **14**, 9796-9806 (2020).
27 Ren, Q. *et al.* Optoelectronic Devices for In-Sensor Computing. *Adv Mater* **37**, e2407476 (2025).
28 Tan, Y. *et al.* A Bioinspired Retinomorphic Device for Spontaneous Chromatic Adaptation. *Adv Mater* **34**, e2206816 (2022).
29 Ng, S. E. *et al.* Retinomorphic Color Perception Based on Opponent Process Enabled by Perovskite Bipolar Photodetectors. *Adv Mater* **36**, e2406568 (2024).
30 Hiramoto, M., Imahigashi, T. & Yokoyama, M. Photocurrent multiplication in organic pigment films. *Appl. Phys. Lett.* **64**, 187-189 (1994).

31 Gao, J. *et al.* Mitigating Dark Current in Photomultiplication Organic Photodetectors via the Charge Trap Gradient Bulk Heterojunction. *ACS Appl Mater Interfaces* **17**, 52426-52434 (2025).
32 Shi, L. *et al.* Atomic-level chemical reaction promoting external quantum efficiency of organic photomultiplication photodetector exceeding 10(8)% for weak-light detection. *Sci Bull (Beijing)* **68**, 928-937 (2023).
33 Lan, Z. *et al.* Near-infrared and visible light dual-mode organic photodetectors. *Sci. Adv.* **6**, eaaw8065 (2020).
34 Li, L. *et al.* Achieving EQE of 16,700% in P3HT:PC71BM based photodetectors by trap-assisted photomultiplication. *Sci Rep* **5**, 9181 (2015).
35 Lan, Z. & Zhu, F. Electrically switchable color-selective organic photodetectors for full-color imaging. *ACS Nano* **15**, 13674-13682 (2021).
36 Tang, X., Ackerman, M. M., Chen, M. & Guyot-Sionnest, P. Dual-band infrared imaging using stacked colloidal quantum dot photodiodes. *Nat. Photonics* **13**, 277-282 (2019).
37 Tang, Y. *et al.* Dual-mode narrowband organic photodetectors for self-aligned imaging in NIR-I and NIR-II. *Nat Commun* **16**, 7144 (2025).
38 Kang, Y., Kim, T. H., Lee, M. J. & Shim, J. W. Dual-Mode Organic Photodetectors with Optimized Charge Dynamics and Barrier Modulation for Superior Spectral Selectivity. *Small* **21**, e2503701 (2025).
39 Han, J. *et al.* Dual‐Polarization‐Sensitive Organic Photodetectors for Real‐Time Polarimetric Imaging. *Laser Photonics Rev.* (2025).
40 Lim, S. J. *et al.* Organic-on-silicon complementary metal-oxide-semiconductor colour image sensors. *Sci Rep* **5**, 7708 (2015).
41 Burgos, S. P., Yokogawa, S. & Atwater, H. A. Color imaging via nearest neighbor hole coupling in plasmonic color filters integrated onto a complementary metal-oxide semiconductor image sensor. *ACS Nano* **7**, 10038-10047 (2013).
42 Kang, H.-S., Lee, M.-J. & Choi, W.-Y. Si avalanche photodetectors fabricated in standard complementary metal-oxide-semiconductor process. *Appl. Phys. Lett.* **90** (2007).
43 Lee, M.-J. & Choi, W.-Y. Effects of Parasitic Resistance on the Performance of Silicon Avalanche Photodetectors in Standard CMOS Technology. *IEEE Electron Device Letters* **37**, 60-63 (2016).
44 He, X. *et al.* A microsized optical spectrometer based on an organic photodetector with an electrically tunable spectral response. *Nat. Electron.* **7**, 694-704 (2024).
45 Zhang, Z. *et al.* Bias-Switchable Dual-Mode Organic Photodetector with High Operational Stability Using Self-Trapped Cs(3)Cu(2)I(5) Interfacial Layer. *Angew. Chem. Int. Ed. Engl.* **63**, e202404067 (2024).
46 Liu, Q. *et al.* Organic photodiodes with bias-switchable photomultiplication and photovoltaic modes. *Nat Commun* **14**, 6935 (2023).
47 Armin, A., Jansen-van Vuuren, R. D., Kopidakis, N., Burn, P. L. & Meredith, P. Narrowband light detection via internal quantum efficiency manipulation of organic photodiodes. *Nat. Commun.* **6**, 6343 (2015).
48 Lin, Q., Armin, A., Burn, P. L. & Meredith, P. Filterless narrowband visible photodetectors.

Nat. Photonics **9**, 687-694 (2015).
49 Xie, B. *et al.* Self-filtering narrowband high performance organic photodetectors enabled by manipulating localized Frenkel exciton dissociation. *Nat. Commun.* **11**, 2871 (2020).
50 Siegmund, B. *et al.* Organic narrowband near-infrared photodetectors based on intermolecular charge-transfer absorption. *Nat. Commun.* **8**, 15421 (2017).
51 Wang, Z., Tang, Y., Han, J. & Zhu, F. Visible-blind near-infrared organic photodetectors. *Appl. Phys. Lett.* **124**, 021103 (2024).
52 Pecunia, V. *et al.* Guidelines for accurate evaluation of photodetectors based on emerging semiconductor technologies. *Nat. Photonics* **19**, 1178-1188 (2025).
53 Ma, Y. *et al.* Amplified narrowband perovskite photodetectors enabled by independent multiplication layers for anti-interference light detection. *Sci. Adv.* **11**, eadq1127 (2025).
54 Lan, Z., Lee, M.-H. & Zhu, F. Recent Advances in Solution-Processable Organic Photodetectors and Applications in Flexible Electronics. *Adv. Intell. Syst.* **4**, 2100167 (2022).
55 Kar, A., Dhara, S. K., Sen, D. & Biswas, P. K. in *Proceedings of the IEEE/CVF Conference on Computer Vision and Pattern Recognition.* 16205-16215.
56 Wagner, F. & Silva, A. Some considerations about Ångström exponent distributions. *Atmospheric Chemistry and Physics* **8**, 481-489 (2008).
57 Silva, M. *YOLO-Parking-Spot: Parking Spot Detection using YOLOv8*, <https://github.com/math-silva/YOLO-Parking-Spot> (2024).
58 Ultralytics YOLO (2023).

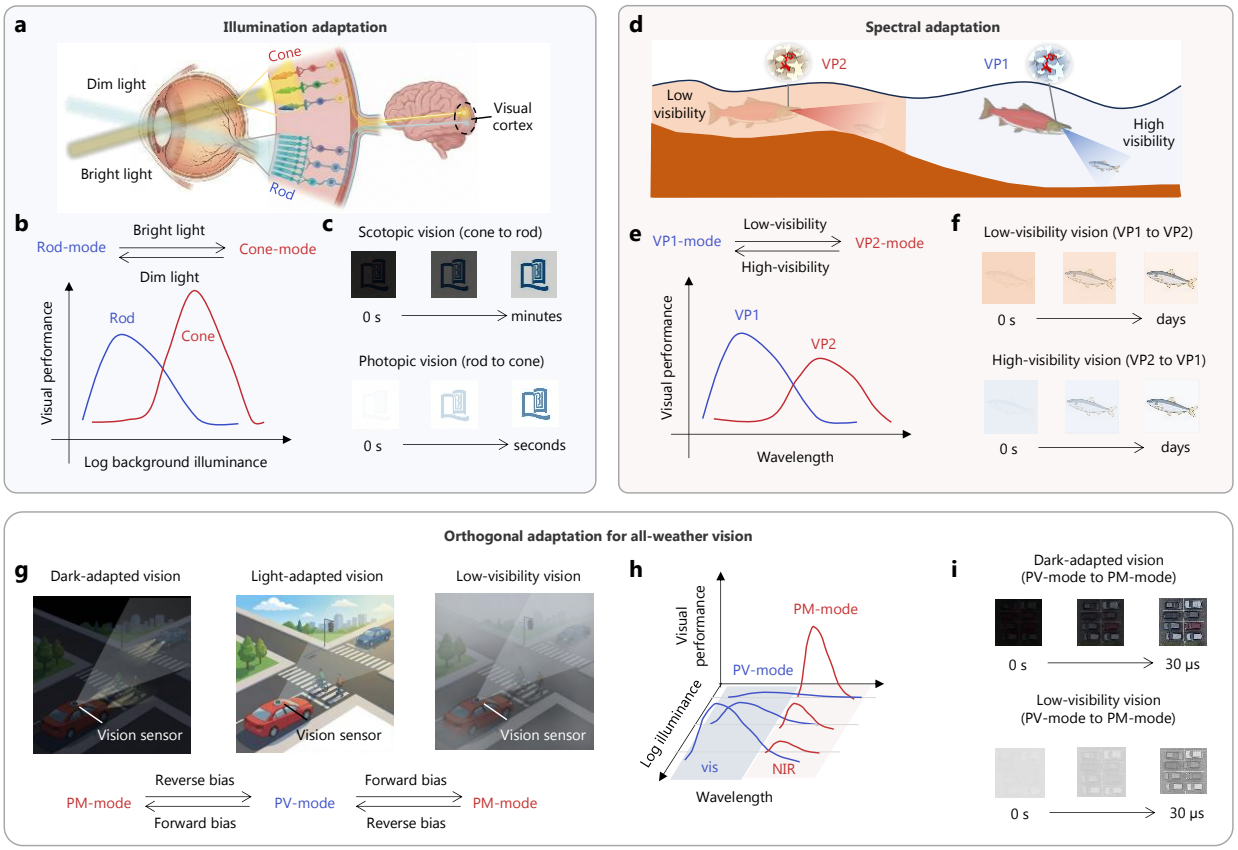


Fig. 1. Bioinspired in-sensor orthogonal adaptation for robust all-weather multispectral vision. a, Schematic of biological illumination adaptation in the human eye. The visual system transitions between rod photoreceptors for scotopic vision in dim light and cone photoreceptors for photopic vision in bright light. **b,** Visual performance of rod and cone photoreceptors as a function of background illuminance. **c,** Visual adaptation process for scotopic (top) and photopic (bottom) visions. **d,** Schematic of biological spectral adaptation in Pacific salmon. The species modulate VP1 and VP2 to optimize contrast in varying water visibility conditions (clear versus turbid). **e,** Spectral response characteristics showing the shift in peak sensitivity wavelength between VP1 and VP2 modes. **f,** Visual adaptation process for varying visibility conditions. **g,** Schematic of the in-sensor orthogonal adaptation for different scenarios. The organic vision sensor electrically reconfigures between a PV mode (forward bias) for high-fidelity light-adapted vision and a PM mode (reverse bias) for high-sensitivity dark-adapted vision. **h,** Visual performance of PV and PM modes of the organic vision sensor array as functions of illuminance and wavelength. **i,** Visual adaptation process for dark-adapted and low-visibility visions.

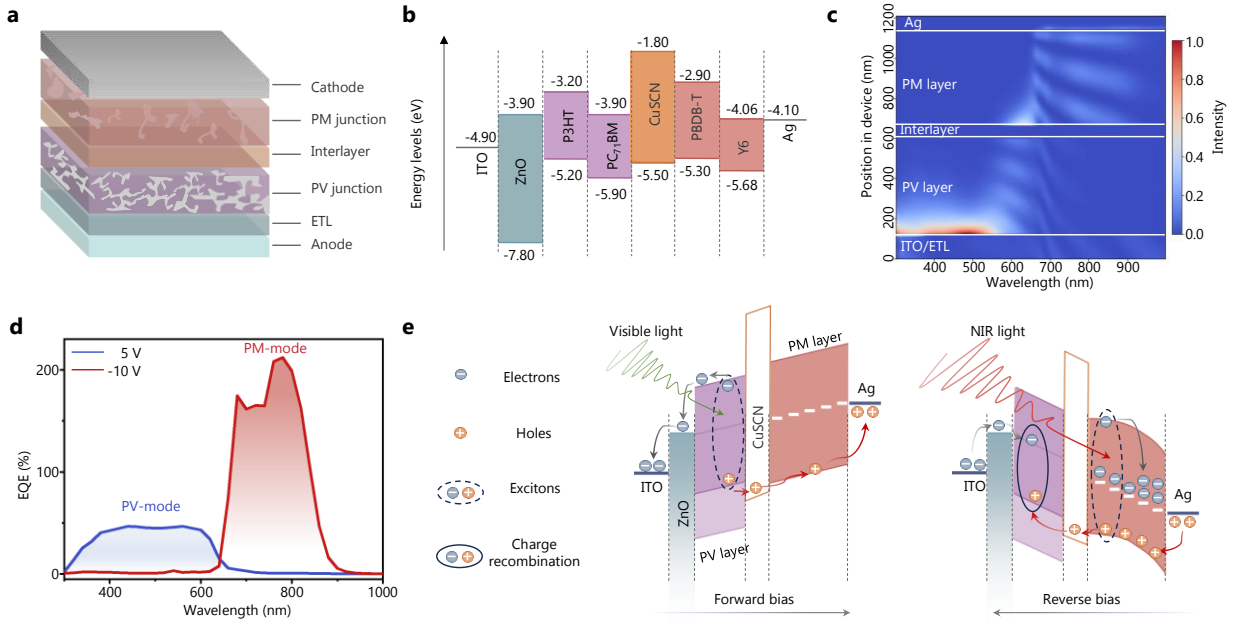


Fig. 2. Spectral responses of PV/PM-OPD. a, Cross-sectional view of the PV/PM-OPD. **b,** Schematic diagram of energy levels of the functional materials used in the device. **c,** Profile of absorbed photon distribution in the PV/PM-OPD. **d,** *EQE* (λ) spectra measured for the PV/PM-OPD operated under a forward bias of 5 V and a reverse bias of -10 V, demonstrating a unique bias-switchable spectral-adapted response capability. **e,** Schematic diagrams illustrate the spectral selective responses of the dual-mode PV/PM-OPD: Under a forward bias, the front PV junction is at its reverse-biased condition, producing a photocurrent by absorbing short-wavelength (visible) light, the rear PM junction is under its forward conduction state, passively conducting current. Under reverse bias, the front PV junction is at its forward conduction state passively conducting current, while the rear PM junction is at its reverse-biased detection condition state, producing a photocurrent by absorbing the long-wavelength (NIR) part of the incoming light.

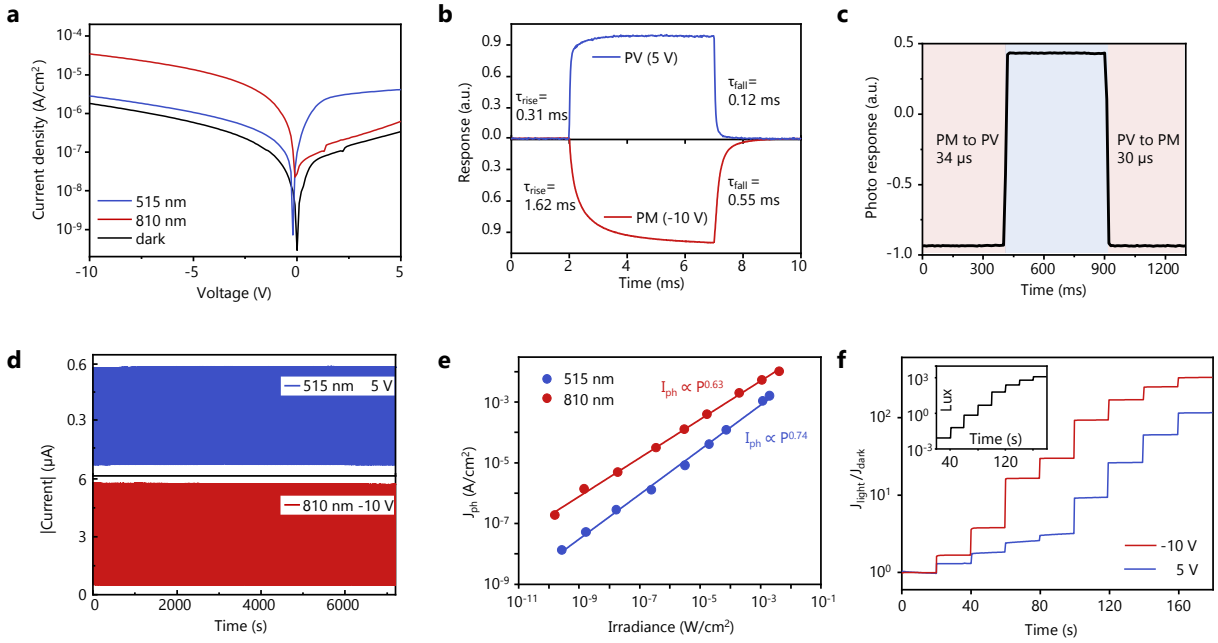


Fig. 3. Characteristics of PV/PM-OPD. a, *J*–*V* characteristics measured for the dual-mode PV/PM-OPD in the dark (black curve), under visible (515 nm) illumination (blue curve), and under NIR (810 nm) illumination (red curve). **b,** Transient photoresponse for the PV mode (5 V, 515 nm) and PM mode (−10 V, 810 nm). **c,** Switching times between PM mode (−10 V) and PV mode (5 V) under white light illumination, shown for both transition directions. **d,** Operational stability of the dual-mode PV/PM-OPD in PV mode (5 V) and PM mode (−10 V), evaluated under repeated illumination with 100 Hz modulated visible light (515 nm, 6.3 µW) and NIR light (810 nm, 1.4 µW) over a period of 7200 s. **e,** LDR of the PV/PM-OPD in PV mode (blue dots, 5 V) and PM mode (red dots, −10 V). **f,** J_{light}/J_{dark} ratio of the dual-mode PV/PM-OPD as a function of halogen lamp illuminance, ranging from 8.4×10^{-3} to 1.2×10^{3} lux, measured at a constant exposure time of 20 s. The inset shows the range of illuminance values used during the measurements.

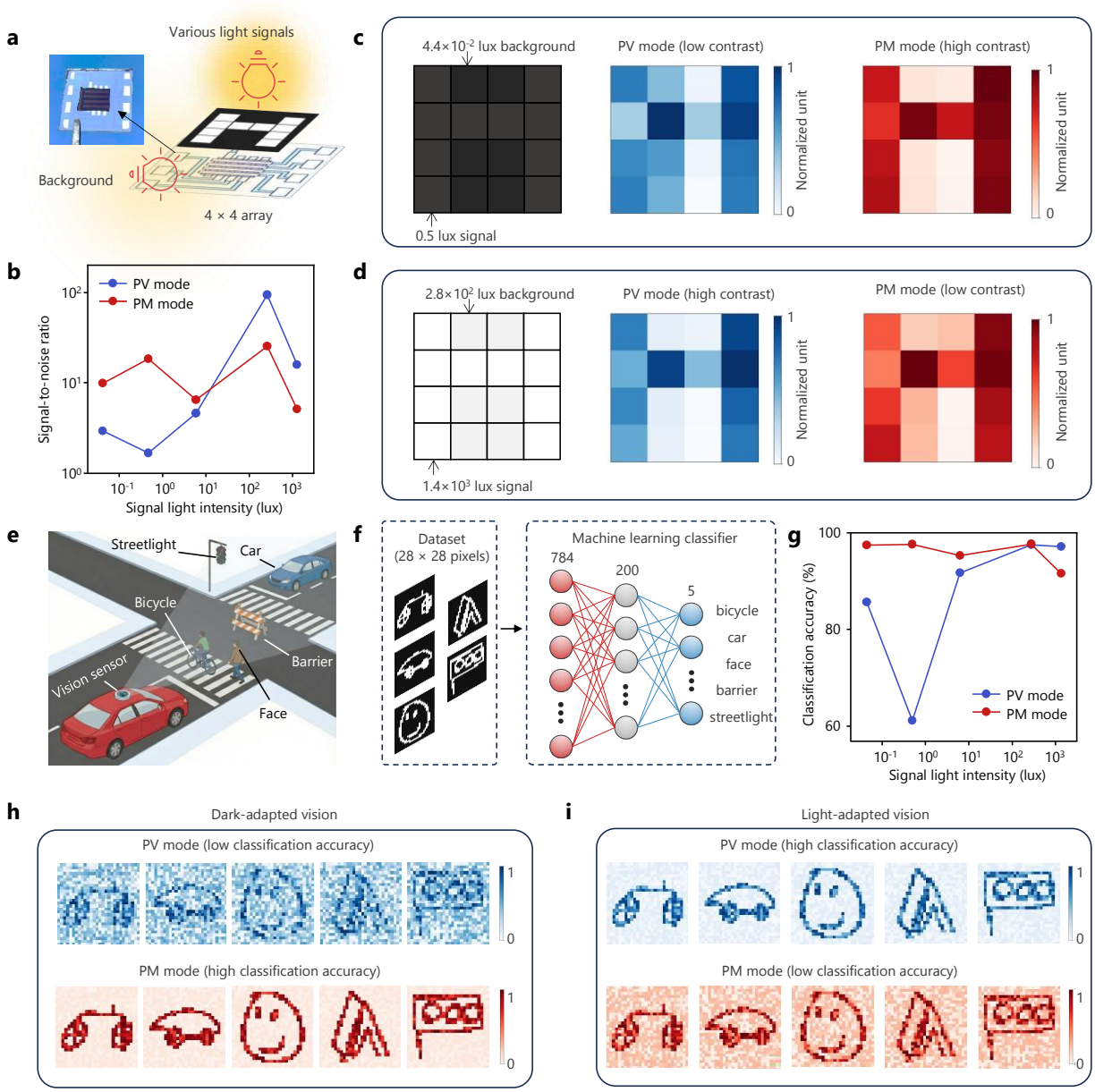


Fig. 4. Illumination adaptation of the dual-mode vision sensor for pattern recognition. a, Schematic of the experimental setup for "H" pattern recognition using a 4 × 4 vision sensor array under different ambient light levels, illustrating imaging performance in both PV and PM modes for dark- and light-adapted conditions. **b**, SNR of the images formed by the sensor array as a function of light intensity. The PM mode (red dots) exhibits superior SNR in low-light conditions, while the PV mode (blue dots) outperforms PM mode at higher light intensities. "H" pattern recognition using a 4 × 4 vision sensor array in both PV and PM modes: under **c**, dark-adapted vision conditions (4.4×10^{-2} lux ambient, 0.5 lux signal) and **d**, light-adapted vision conditions (2.8×10^{2} lux ambient, 1.6×10^{3} lux signal). **e**, Illustration of the traffic scenario used for the system-level simulation, containing five object classes of bicycle, car, face, barrier, and streetlight. **f**,

Architecture of the machine learning classifier trained on the “Quick Draw!” dataset to classify 28 × 28-pixel images into the five target categories. **g**, Simulated classification accuracy as a function of light intensity. Representative simulated images using both PV and PM modes under **h,** dark-adapted vision and **i**, light-adapted vision scenarios.

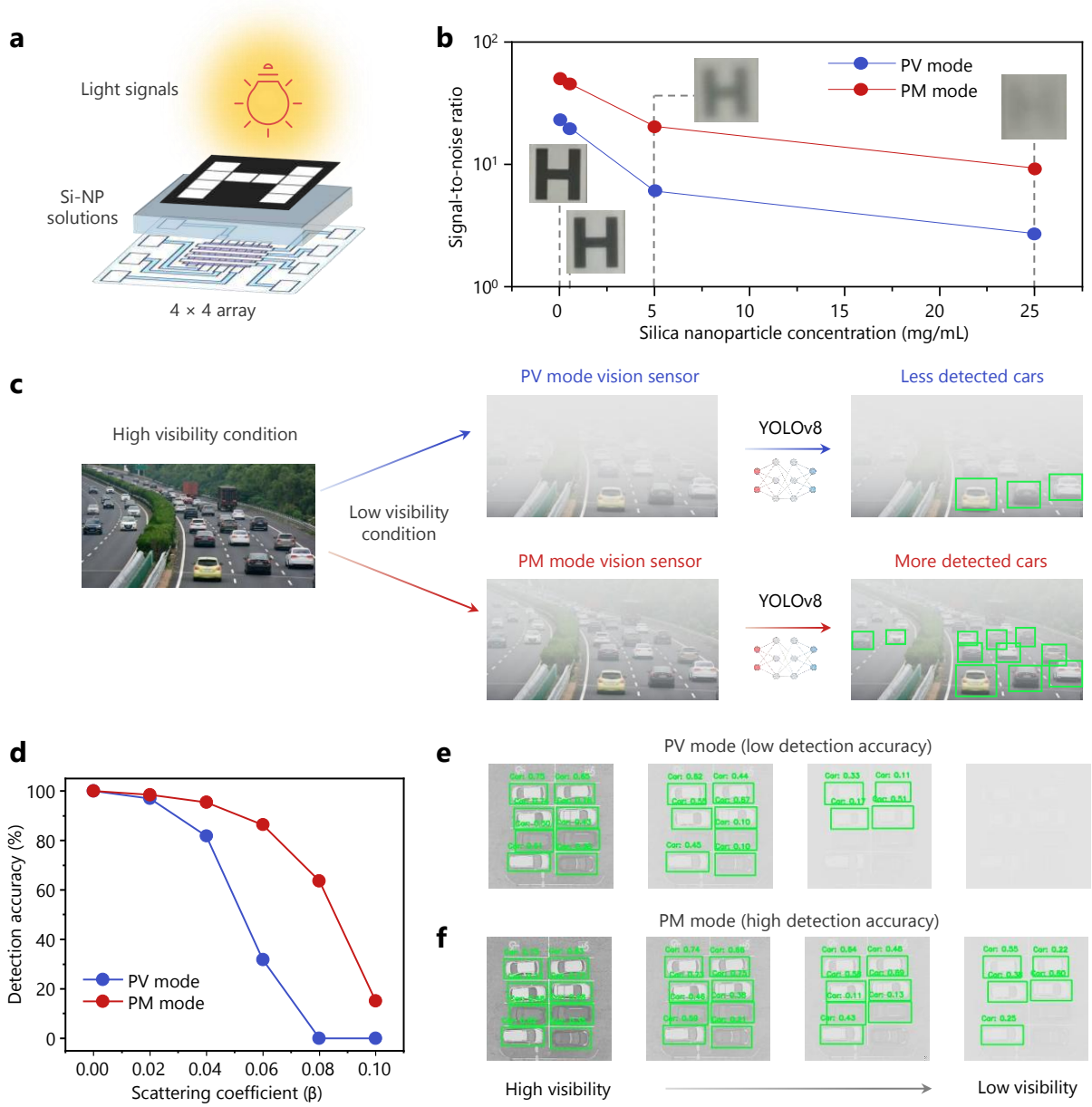


Fig. 5. Spectral adaptation of dual-mode vision sensor for low-visibility vision. a, Schematic of the experimental setup for recognizing an "H" pattern with a 4 × 4 vision sensor array, where visibility is modulated by varying the concentration of Si-NPs in the scattering medium to simulate fog or haze. **b**, SNR of "H" pattern images as a function of Si-NP concentration in the scattering layer. Across increasing turbidity, the vision sensor in PM mode (red dots) maintains a higher SNR than in PV mode (blue dots), due to enhanced NIR light penetration. Insets: Corresponding images of the "H" pattern captured in each mode at varying Si-NP concentrations. **c**, Simulated spectral-adapted images illustrating the performance of the dual-mode vision sensor (PV and PM modes) under low-visibility conditions. **d**, Vehicle detection accuracy as a function of scattering coefficient (β), indicating decreasing visibility with increasing β. Representative images formed in

(**e**) PV mode and (**f**) PM mode show vehicle identification (green rectangles) by the dual-mode vision sensor in a parking lot under varying visibility conditions.

Supplementary Files

This is a list of supplementary files associated with this preprint. Click to download.

- SupplementaryInformation.docx